Composite Structures 311 (2023) 116845

Contents lists available at ScienceDirect

Composite Structures

journal homepage: www.elsevier.com/locate/compstruct

Improving the crashworthiness of CFRP structures by rubbery nanofibrous interlayers

Maria Pia Falaschetti [a,c,*], Francesco Rondina [a], Emanuele Maccaferri [b], Laura Mazzocchetti [b,c], Lorenzo Donati [a,c], Andrea Zucchelli [a,c], Loris Giorgini [b,c]

[a] Department of Industrial Engineering, University of Bologna, Viale Risorgimento 2, 40136 Bologna, Italy
[b] Department of Industrial Chemistry "Toso Montanari", University of Bologna, Viale Risorgimento 4, 40136 Bologna, Italy
[c] Interdepartmental Center for Industrial Research on Advanced Applications in Mechanical Engineering and Materials Technology, CIRI-MAM, University of Bologna, Viale Risorgimento 2, 40136 Bologna, Italy

ARTICLE INFO

Keywords:
Crashworthiness
CFRP
Nanofibers
Rubber
Electrospinning
Specific energy absorption

ABSTRACT

Crashworthiness is the capability of a component to dissipate impact energy throughout its deformation and failure. Composite materials are used to produce crashworthy components to ensure vehicle safety, thanks to their ability to dissipate a high energy amount while maintaining a low weight. The present work investigates the integration of rubbery nanofibers within the laminate interlayers to enhance crush performance. Three different thicknesses (10, 20, and 40 μm) of nanofibrous mats made by nitrile butadiene rubber and polycaprolactone (NBR/PCL) blends were produced by single-needle electrospinning technique and integrated into the laminates during the hand-layup. Mechanical properties of the nano-modified laminates are compared to the reference configuration: the effect of the interlayers is evaluated by Double Cantilever Beam (DCB) and End-Notched Flexure (ENF) interlaminar fracture tests. At the same time, the specific crush energy absorption (SEA) is measured by the compression of self-supporting corrugated specimens. Results show that NBR/PCL nanofibers significantly increase the interlaminar fracture toughness (up to +254% for Mode I and +47% for Mode II), which ultimately helps to improve the total SEA up to +8.2%. The best SEA enhancement is achieved already with a 10 μm nanofibrous membrane while integrating the highest thickness mat has a detrimental effect.

1. Introduction

Composite materials are extensively used in different industrial fields thanks to their appealing mechanical and physical properties, making them suitable for developing lightweight structures requiring high strength and stiffness. In particular, composites made of carbon fiber and epoxy resin have been widely used in crashworthy applications, thanks to their well-established capability for energy absorption in the event of a crash [1,2]. In these scenarios, the combination of high-strength and brittle fibers with tough polymeric matrices causes the fragmentation of the structure into small debris [3], ultimately resulting in high energy dissipation. This phenomenon is determined by extensive fracture propagation at the micro- and meso-scale and subsequent high frictional shear forces at the crack surfaces caused by compression [4,5]. The correct design and control of the fragmentation zone evolution ultimately determine a stable and safe outcome of the crash event.

The progressive and stable crushing can be obtained by designing and manufacturing a proper trigger. Whereas crash-absorbing aluminum profiles are provided with a crimp to facilitate folding, composite components usually present a machined bevel or sawtooth profile at the free edge [6]. Alternatively, a ply-drop-off is introduced at a specific profile height, in case the free edge cannot be left exposed [7]. Indeed, composite structures designed with a proper triggering mechanism will fragment in a controlled manner if subjected to compressive forces and are shown to absorb up to twice the energy per unit mass of equivalent aluminum components [7].

A combination of multiple design variables determines the resulting crush behavior at a macroscopic level: experimental studies have investigated the effect on energy absorption of section geometry [8–11], design of the trigger region [6,7], stacking sequence [12,13], and individual components of the composite [14–16], but a unique assessment of the effect of these parameters is far from established, and a comprehensive guideline for the optimization and prediction of the crush behavior has been an ongoing research effort [17].

* Corresponding author at: University of Bologna, Department of Industrial Engineering, via Fontanelle 40, 47121 Forlì (FC), Italy.
E-mail address: mariapi.falaschetti2@unibo.it (M.P. Falaschetti).

https://doi.org/10.1016/j.compstruct.2023.116845
Received 15 October 2022; Received in revised form 26 December 2022; Accepted 16 February 2023
Available online 22 February 2023

The proper execution of experimental tests to evaluate the Specific Energy Absorption (SEA) of a component is also of crucial importance: self-supporting geometries do not require specialized testing equipment and provide insights into the behavior of the final design of the structure; however, evaluating different geometries requires significant effort on tooling and expensive manufacturing labor. On the other hand, flat coupons are easy to manufacture and can be tested quickly; however, their SEA is significantly influenced by the configuration of the supporting fixture [8]. For these reasons, the use of flat coupons is limited to comparative campaigns where multiple configurations have to be tested in a short time [18,19].

Over the years, multiple self-supporting profile geometries have been evaluated to remove the supporting fixture's influence from the test data. Among these, some geometries are also found in real engineering applications: circular tubes with different cross-sections [9,12], truncated cones [10], and corrugated profiles [11,20]. The latters' cross section geometry consists of tangentially joined arc segments, usually called waves; the arc radius can vary from 0° (actually corresponding to flat coupons) up to 180°, equivalent to repeating semicircumferences. In [20], Hanagud et al. concluded that this last configuration have the highest sustained crush stress among all the investigated geometries. Moreover, it does not have perimeter constraint, such as a tubular specimen [21] and has lower manufacturing costs than other test methods commonly used for SEA characterization [11].

The ideal crush mechanism has been demonstrated to be a compromise between brittle fracturing and lamina bending [22,23], and it was found that the matrix mainly controls such behavior. In crush applications, matrix failures generate interlaminar cracks and plies separations, resulting in an unfavorable collapse, ultimately leading to a lower energy absorption than the fragmentation mode [16,19,23,24].

In addition, several studies demonstrated that a tough matrix could lead to a higher crushing energy dissipation [10,23,24]. For example, according to Cauchi Savona et al. [8], materials with a lower Mode I and Mode II fracture toughness absorb lower crushing energy. Moreover, the authors found that fracture toughness propagation properties are more closely correlated to the energy absorption values than initiation toughnesses and that Mode II has a more predominant role, suggesting a prevalence of shear-cracking failure mode against opening mode (Mode I).

Many attempts to enhance matrix properties are found in the literature, in particular Mode I and Mode II fracture toughnesses. Different methods have been pursued to improve the matrix toughness: the addition of thermoplastic resin additives [25,26], through-the-thickness stitching [27,28], and layer interface reinforcements [29,30] are some examples. It has been demonstrated that while these methods increase toughness, they may carry other disadvantages. Adding rubber or thermoplastic powder to the matrix bulk may increase its viscosity leading to production issues (a crucial parameter when working with some production technologies, e.g., Resin Transfer Moulding) [31]. At the same time, stitching can create in-plane damage and undesired resin-rich areas [32,33]. Among interface reinforcements, films [31] and nanofibrous membranes [34] can be distinguished. In the last twenty years, the use of nanofibers as composite toughener enhancers is spreading thanks to their ability to improve the interlaminar fracture toughness without significantly increasing laminate weight and dimensions. Moreover, mats with randomly-oriented nanofibers can be produced, resulting in an isotropic interface reinforcement.

Many different materials have been evaluated as nanofibrous membrane layers: polycaprolactone (PCL) [29,35], Nylons [29,36], polyvinylidene fluoride (PVDF) [35,37], and elastomeric nanofibers [30]. The reasons for the development and the widening use of nanofibers are their large aspect ratio, high surface-to-volume ratio, and ease of integration into the polymer matrix [38]. Rubbery nanofibrous membranes for composite modification represent a recent smart way to enhance interlaminar fracture toughness and damping [34,36]. Unfortunately, rubbery materials cannot be shaped into nanofibers easily. Any attempt to electrospin uncrosslinked "liquid" rubber leads to a homogenous film within a few minutes after the spinning process due to the rubber's cold flow occurring above the glass transition (T_g) [39]. For this reason, most literature reports just proofs-of-concept or the production of rubbery fibers with large diameters [40–43]. Moreover, rubber crosslinking is usually necessary to maintain the fiber shape [41,43,44]. Recently, the production of uncrosslinked rubbery nanofibers via single-needle electrospinning of nitrile butadiene rubber and poly(ε-caprolactone) (NBR/PCL) blends [39] was reported. Such nanofibers are dimensionally stable even when a significant fraction of NBR is loaded, and the resulting mat can be easily integrated between prepreg plies during the lamination step. NBR/PCL nanofibers were shown to significantly improve the interlaminar fracture toughness of CFRP Mode I and Mode II; in particular, the blend with 60%wt NBR showed the best outcome [36]. However, the effects on the SEA of crashworthy composite structures are still unexplored. Hence, in the present work, compressive crush tests of self-supporting coupons [11,45,46] were performed on pristine and NBR/PCL nano-reinforced epoxy-based CFRP laminates. Rubbery nanofibers were electrospun from an NBR/PCL blend with 60% rubber weight fraction and integrated into the composite during the lamination step. Three different mat thicknesses (10, 20, and 40 μm), roughly equivalent to 5, 10, and 20 g/m^2, were produced and their effect on SEA was evaluated. In addition, the obtained SEA values were compared with the interlaminar fracture toughness determined by DCB and ENF tests to understand their correlation.

2. Materials and methods

2.1. Materials

Carboxylated nitrile butadiene rubber (NBR) NIPOL 1072CGX was purchased from Zeon Chemicals [68%mol butadiene (Bu), 28%mol acrylonitrile (ACN), 4%mol methacrylic acid (MAA)]. Poly(ε-caprolactone) (PCL, $M_w = 70–90$ kDa), *N,N*-dimethylacetamide (DMAc), *N,N*-dimethylformamide (DMF), and chloroform ($CHCl_3$) were purchased from Sigma-Aldrich and used without further purifications. GG204P IMP503Z-HT carbon/epoxy plain weave prepreg (200 g/m^2 carbon fabric) was supplied by G. Angeloni s.r.l. (Venezia, Italy).

2.2. Nanofibrous mat and CFRP laminate production

The solution blend for the electrospinning process is prepared by mixing NBR and PCL solutions to obtain a final NBR/PCL 60:40 wt ratio in the nanofibers. This rubber/thermoplastic proportion provides a stable membrane over a long time which is also easy to handle during lamination [34,36] and is expected to demonstrate better enhancement for the crashworthiness material property.

Nanofibrous mats are produced via the single-needle electrospinning technique employing a Spinbow electrospinning machine equipped with four syringes. Fibers are collected on a rotating drum covered with poly (ethylene)-coated paper at 50 rpm (0.39 m/s tangential speed) to obtain randomly-oriented nanofibers. Mats have final dimensions of approximately 30×40 cm. More details regarding the production procedure can be found in [39].

Three different membrane thicknesses are produced: 10, 20, and 40 μm. These values represent the average mat thickness obtained by only varying electrospinning times. It is to underline that the quantification of the mat thickness depends on the pressure applied during the measurement, as discussed in [47]. The present thicknesses were measured using an analog indicator under a pressure of 35 kPa. Such thicknesses roughly correspond to 5, 10, and 20 g/m^2 mat grammage. Lower thicknesses and, therefore, grammages are not recommended due to the difficulty of handling a single mat during the hand-lay-up.

The process of interleaving a nanofibrous mat is similar to that of prepreg hand-layup: the mats are handled and cut with their supporting paper to retain the planar shape and are placed onto the laminate stack,

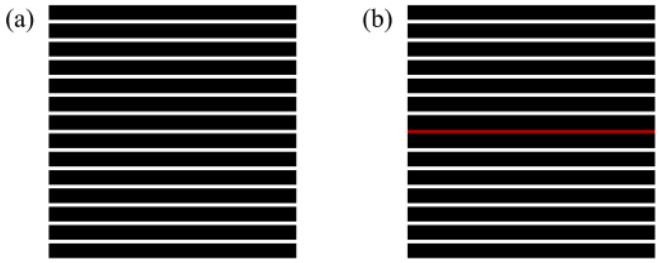

Fig. 1. DCB and ENF coupon stacking sequence showing CFRP plies in black, nanofibrous mat in red: (a) reference laminate and (b) nano-reinforced laminates.

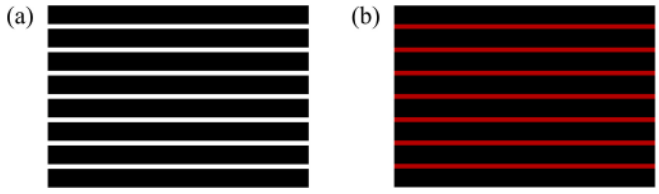

Fig. 2. Compressive crush coupon stacking sequence showing CFRP plies in black, nanofibrous mat in red: (a) reference laminate and (b) nano-reinforced laminates.

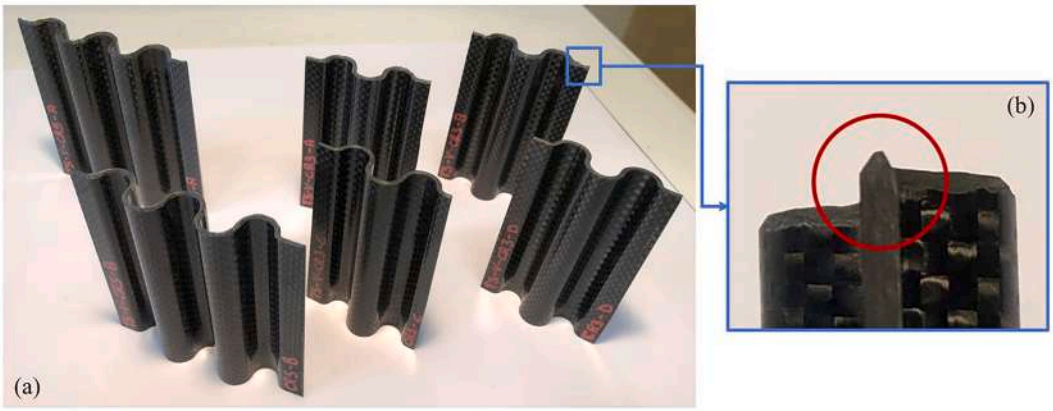

Fig. 3. (a) Self-supporting corrugated specimens: 2 CR5 specimens on the left, 4 CR3 coupons on the right; (b) detail of the central chamfer trigger.

mating the mat with the ply below. Upon contact, the mat adheres to the uncured resin, and, once the nanofibrous mat is fully adhered, the support paper can be safely peeled off and the next ply is laminated above it.

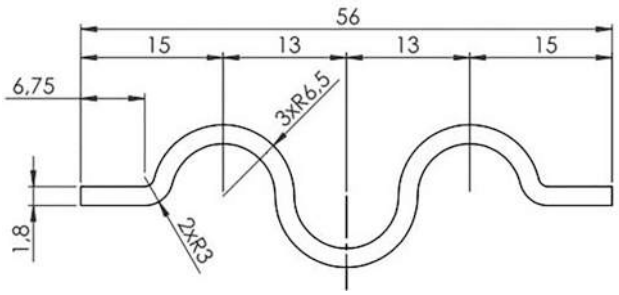

Fig. 4. Drawing of the CR3 profile geometry section, all dimensions are in mm.

Reference DCB and ENF coupons are produced from a single plate according to ASTM D5528 and ASTM D7905 [48,49] guidelines, respectively. A stacking sequence of 14 carbon/epoxy prepreg layers is chosen (Fig. 1a), which yields a cured plate thickness of 3.7 mm. Nano-reinforced coupons are obtained using the same stacking sequence of the reference coupons, adding a nanofibrous mat at the central interface (Fig. 1b). In all configurations, a PTFE release film of 16 μm thickness is inserted at the midplane to obtain a pre-crack. The position of the release film is marked on the plates so that all specimens can be later cut to 50 mm effective initial crack length.

Self-supporting corrugated crush specimens are fabricated by hand layup of eight CFRP plies using a dedicated semi-closed mold. Reference and nano-reinforced specimens are produced (Fig. 2); the latter is obtained by interleaving a nanofibrous mat between each interface.

To improve the embedding between nanofibers and epoxy, the nano-

reinforced laminates must go through a preliminary heat treatment phase of 2 h at 40°C under vacuum right before curing. In order to remove possible sources of difference, the reference samples have also been heat treated under the same condition. The following resin cure cycle for the prepreg is 2 h at 135°C with 6 bar pressure, heating and cooling ramps of 2°C/min.

The profile geometry for the self-supporting corrugated coupons was firstly introduced by Feraboli [11]. Here, two different shapes have been manufactured and tested (Fig. 3a): one with 3 semicircle repetitions (named CR3) and one with 5 repetitions (named CR5). A 45° central chamfer trigger is machined on the loading edge of the specimens by means of a Dremel mill equipped with a diamond tool (Fig. 3b). Nominal section dimensions are reported in Fig. 4 for the CR3 geometry; specimen height is 80 mm for all samples.

3. Experimental tests

All tests were carried out using a servo-hydraulic universal testing machine equipped with a 100 kN load cell for crush tests, a 200 N load cell for DCB, and a 10 kN one for ENF tests.

All tests listed in Table 1 are performed under displacement control: DCB and ENF tests are carried out at 5 mm/min and 2 mm/min loading rates, respectively, as prescribed by the relevant ASTM references [48,49], while crush specimens are tested at 5 mm/min.

DCB tests allow the evaluation of the Mode I energy release rate (G_I). The energy release rate for the initiation and the propagation stages ($G_{I,C}$ and $G_{I,R}$, respectively) are calculated using (1):

$$G_{I,i} = \frac{3P_i\delta_i}{2ba_i} \tag{1}$$

where $G_{I,i}$ is the energy release rate (J/m^2), P_i is the load (N), δ_i is the displacement (mm), a_i is the crack length (mm), and b is the specimen width (mm).

ENF tests are performed to measure the Mode II fracture toughness (G_{II}). The fracture toughness at the initiation and propagation stages ($G_{II,C}$ and $G_{II,R}$, respectively) are calculated using (2):

$$G_{II,i} = \frac{9P_i\delta_i{a_i}^2}{2b\left(\frac{1}{4}L^3 + 3{a_i}^3\right)} \tag{2}$$

where $G_{II,i}$ is the fracture toughness (J/m^2), P_i is the load (N), δ_i is the displacement (mm), a_i is the crack length (mm), L is the span between fixture supports, and b is the specimen width (mm).

The principal outputs of compressive crush tests are the Energy Absorption (EA) and the Specific Energy Absorption (SEA). No standard has yet been formulated to calculate these quantities consistently, consequently comparison and evaluation across multiple works is often challenging. In this work, the EA, function of the stroke length x_c is defined as:

Table 1
Experimental tests.

Test	Configuration		Repetitions
DCB (ASTM D5228)	Reference		3
	Nano-reinforced	10 μm	3
		20 μm	3
		40 μm	4
ENF (ASTM D7905)	Reference		4
	Nano-reinforced	10 μm	3
		20 μm	3
		40 μm	4
Compressive crush	Reference		4 CR3 + 2 CR5
	Nano-reinforced	10 μm	4 CR3 + 2 CR5
		20 μm	4 CR3 + 2 CR5
		40 μm	4 CR3 + 2 CR5

$$EA(x_c) = \int_0^{x_c} f(x)dx \tag{3}$$

with $f(x)$ being the istantaneous sustained crush force.

The total SEA becomes:

$$SEA_T(x_c) = \frac{EA(x_c)}{mx_c/h} \tag{4}$$

where m and h are the the coupon weight and height, respectively.

A different quantity that is often found in the literature is the Steady-State SEA, which is computed from:

$$SEA_{ss}(x_c) = \frac{\int_{x_0}^{x_c} f\left(x\right)dx}{m(x_c - x_0)/h} \tag{5}$$

where additionally, x_0 is an initial displacement value for computation of the steady state SEA, chosen to exclude the transition region before onset of the sustained crush load.

4. Results and discussion

4.1. Interlaminar fracture toughness

As previously discussed, G_I and G_{II} are calculated at both initiation and propagation steps. The initiation value is identified by the first load drop in the load–displacement curve and corresponds to the first crack growth. The propagation values are calculated at all the subsequent load peaks, corresponding to additional delamination growths. Fig. 5 shows the load–displacement curves obtained in DCB tests.

Due to the nature of woven composites, the load–displacement curves of DCB tests show the typical load drops associated with discrete jumps in crack growth. For this reason, it is helpful to distinguish the initiation fracture toughness value from the multiple propagation ones. It can be observed that the addition of nanofibrous reinforcement mats leads to higher sustained loads compared to the reference, and corresponding higher fracture toughness ($G_{I,i}$, as shown in Fig. 6). Furthermore, all nano-reinforced samples show an increasing trend in fracture toughness as the crack length increases due to the promotion of fiber bridging and the generation of multiple fracture surfaces, as observed from SEM micrographs reported in Section 4.4.

The energy release rate at fracture propagation is reported on the left side of Fig. 6 for all the tested coupons, while the initiation ($G_{I,C}$) and propagation ($G_{I,R}$) average values are shown on the right side. Mean

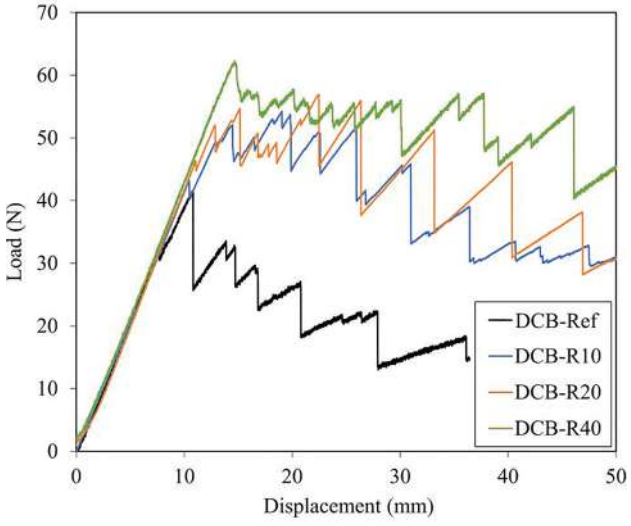

Fig. 5. Load-displacement curves for the DCB tests (one representative curve for each group is shown).

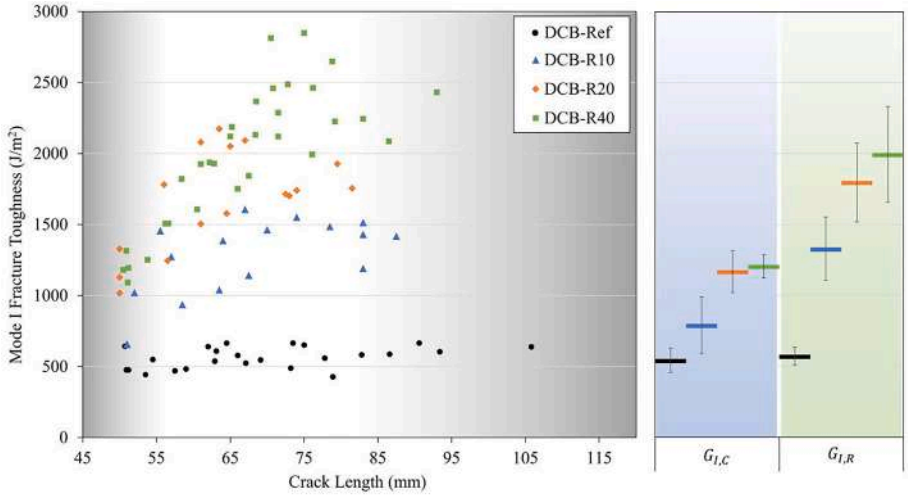

Fig. 6. DCB tests: energy release rate at fracture propagation for all coupons. All data points are on the left, average group values are on the right. One standard deviation on error bars.

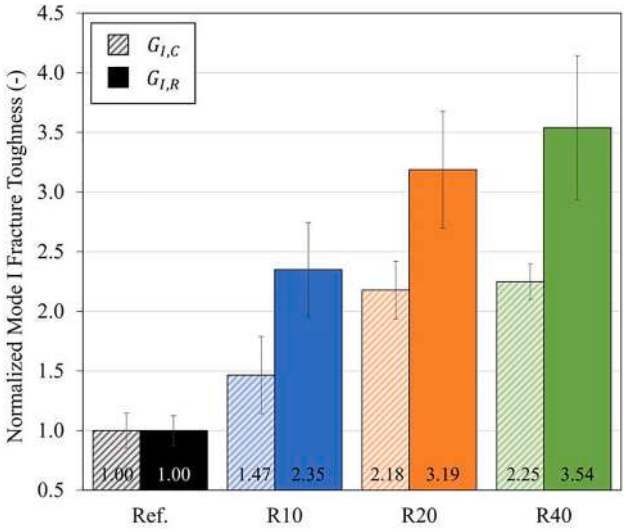

Fig. 7. DCB tests: normalized initial ($G_{I,C}$) and propagation ($G_{I,R}$) Mode I fracture toughness. One standard deviation on error bars.

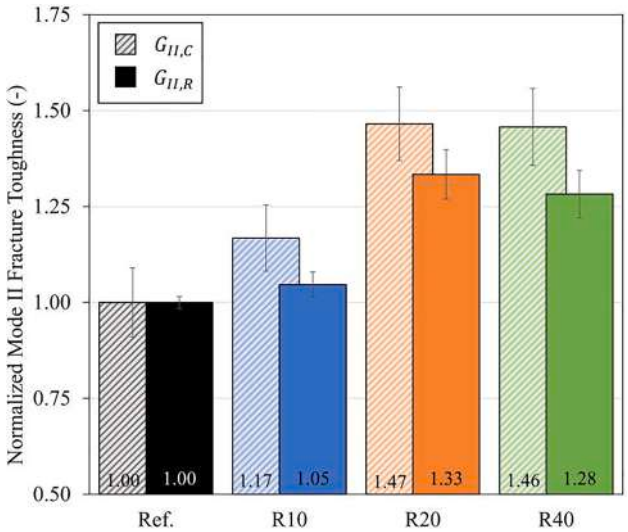

Fig. 8. ENF tests: normalized initial ($G_{II,C}$) and propagation ($G_{II,R}$) Mode II fracture toughness. One standard deviation on error bars.

values for the propagation fracture toughness are calculated in the 55–85 mm crack length region. Both $G_{I,C}$ and $G_{I,R}$ show higher values for the rubbery reinforced coupons compared to the unreinforced ones. The gap between the G_I of unmodified laminate and the one with 10 μm mat is around 250 J/m^2 and 750 J/m^2 for the initiation and the propagation energy release rates, respectively. The increment gets higher with thicker nanofibrous mats: around 620 J/m^2 and 1220 J/m^2 for the initiation and the propagation energy release rates for the 20 μm mat, while, in the case of the 40 μm mat, it reaches 660 J/m^2 and 1420 J/m^2, respectively. In order to highlight the effect of the rubbery interface, results are normalized to the reference unreinforced sample in Fig. 7.

An increasing trend of the interlaminar fracture toughness can be noticed for increased mat thickness, especially in propagation. For example, the Mode I fracture toughness for a coupon with a 10 μm thick nanofibrous mat is increased by 135% the value of the reference material. Moreover, the increment reaches 254% for the fracture propagation in the sample with 40 μm mat, resulting in the best performance, while the difference between the laminates with 20 and 40 μm mats is not significant.

A similar trend is observed for the Mode II interlaminar fracture measured by the ENF tests; however, in this case, the $G_{II,C}$ is always higher than the corresponding $G_{II,R}$ for all rubbery-modified laminates. As shown in Fig. 8, even the thinnest reinforcement can improve the interlaminar fracture toughness, but the effect is more evident with 20 and 40 μm interleaves, with a 50% increase compared to the reference configuration. The described results align with the outcomes in [36], confirming the reliability of this enhancement procedure for interlaminar fracture toughness.

4.2. Crashworthiness SEA

The sustained load curves for the compressive crush tests are reported in Fig. 9 for CR3 (left) and CR5 (right) groups, where only one representative curve per sample is displayed to improve readability. Due to their wider profile section, the load–displacement curves for CR5 samples have a higher sustained load than the CR3 groups. It can be immediately seen that the 10 and 20 μm nano-reinforced crushed specimens have a higher sustained load compared to the reference and 40 μm ones.

SEA values are calculated from Eqs. (4) and Eqs. (5) (with x_c equal to

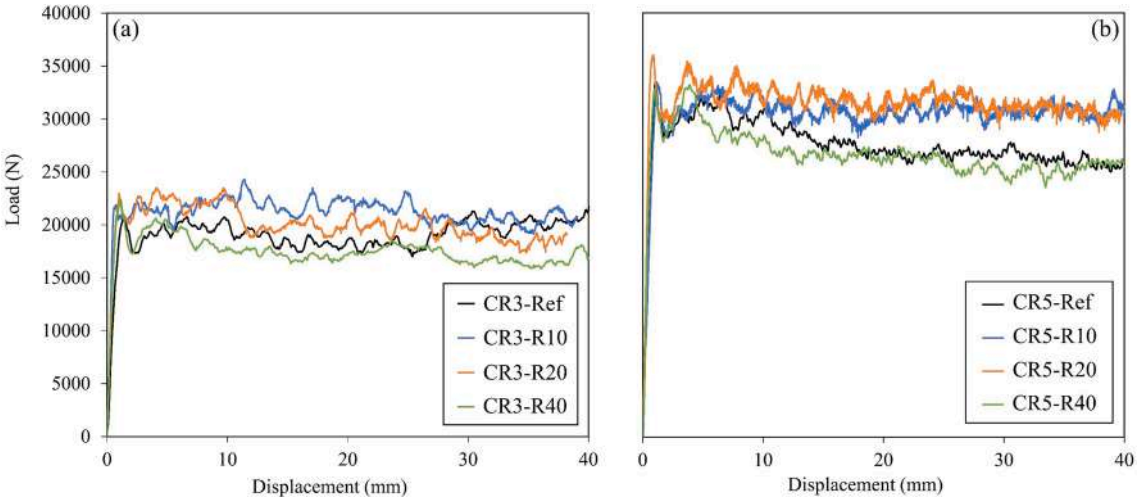

Fig. 9. Compressive crush tests: load–displacement curves for (a) CR3 and (b) CR5 coupons (one specimen representative of each group is shown).

Table 2
Total and Steady-State SEA values for corrugated compressive crush specimens: average value (μ) and standard deviation (σ).

			SEA (J/g)			
			Total		Steady-State	
			μ	σ	μ	σ
Reference		CR3	87.5	2.8	88.6	3.3
		CR5	85.4	–	85.7	–
Nanoreinforced	10 μm	CR3	95.6	2.0	96.9	2.1
		CR5	90.5	–	91.9	–
	20 μm	CR3	93.2	0.7	94.1	1.2
		CR5	93.9	–	94.8	–
	40 μm	CR3	80.4	0.8	80.4	1.0
		CR5	79.7	–	79.3	–

33 mm) and collected in Table 2 for both CR3 and CR5 geometries. The maximum variation between the Total and the Steady-State SEA is around 1%; therefore, only Total SEA values will be addressed from this point on. The SEA for the 40 μm group is lower than the value of the reference group, while the thinner mats lead to an improvement. In particular, for the CR3 geometry, the average values for 10 and 20 μm configurations are 95.6 J/g and 93.2 J/g, respectively, higher than the reference baseline at 87.5 J/g, while it is even lower, 80.4 J/g, for the 40 μm case.

Fig. 10 presents the curves of the EA/m (Energy Absorption normalised to the specimen mass). These allow the evaluation of the geometry's influence on the component's crashworthy behavior. The enlargement of the graph underlines the performance of the different specimens. In particular, as already observed for SEA values, R40 samples result in lower values for both CR3 and CR5 geometries, while R10 and R20 curves are stiffer and mostly superimposable. The CR5 curves, represented in 'solid' colours, show a similar distribution to the CR3s (in lighter colour) of the same group. This justifies the interchangeability of the two geometries [46].

In Fig. 11, the average mass and the absorbed energy (as calculated from Eq. (3)) values for each configuration are normalized to the reference. Normalization has been applied to for CR3 and CR5 geometries to compare each configuration as a single data point. The graph shows the increase of specimen mass with the addition of nanofibrous mats, comparing it with the normalized absorbed energy. It is observed that in the case of low-weight nanofibrous mats, R10 and R20, the absorbed energy is higher than in the references. On the other hand, in

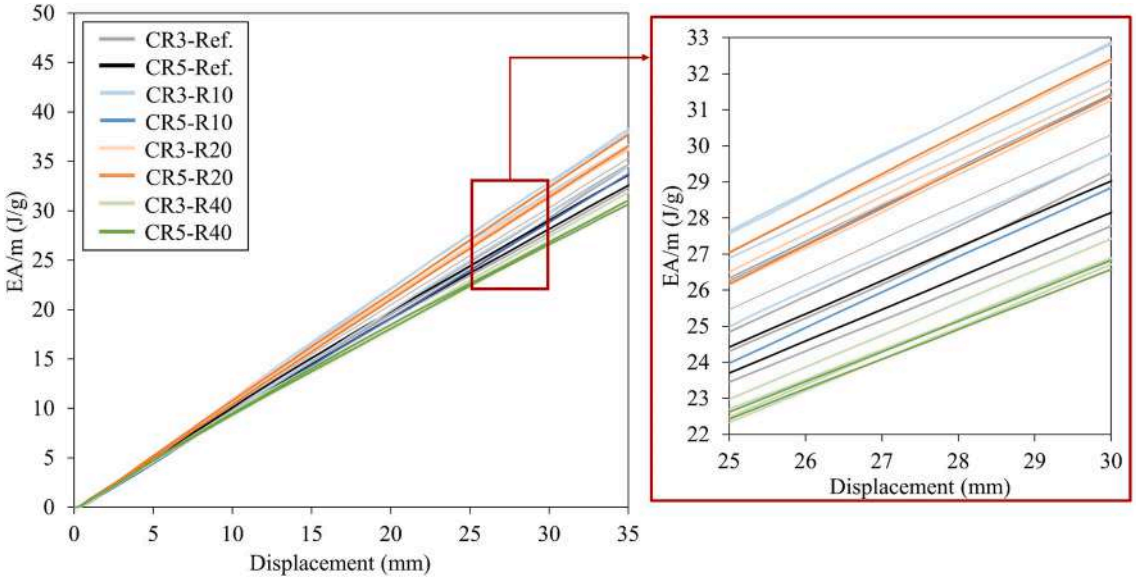

Fig. 10. EA/m curves for every tested specimen. Each group is shown with a different colour.

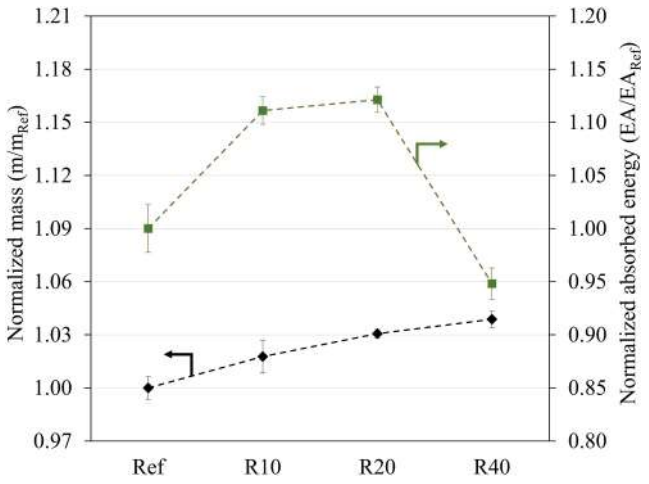

Fig. 11. Compressive crush tests: normalized mass (left axis) and normalized absorbed energy (right axis).

Table 3
SEA results for corrugated compressive crush specimens: average value (μ) and standard deviation (σ).

		Total SEA (J/g)		Normalized Total SEA (%)	
		μ	σ	μ	σ
Reference		86.8	2.6	100.0	3.0
Nano-reinforced	10 μm	93.9	2.9	108.2	3.1
	20 μm	93.4	0.8	107.6	0.8
	40 μm	80.2	0.8	92.3	1.0

the case of the highest grammage, R-40, the absorbed energy is lower.

Finally, Table 3 reports the average SEA values for each material configuration and averaging both geometries; the values on the last two columns are normalized to the reference configuration. It is once again evident that the 10 μm and 20 μm reinforcement mats provide an improvement of the SEA, up to 8.2% compared to the non-modified material. On the contrary, the penalty of using the thickest mat (40 μm) can be quantified in a performance loss near 8%. Furthermore, the thicker mats reduce the scatter of the results, as the standard deviation for the 20 μm and 40 μm configurations is significantly lower than the reference and 10 μm. This effect can be justified by the improved adhesion between the plies, obtained using the nano-reinforcements, which is only partly guaranteed with the lowest thickness. Therefore, the SEA increment has been demonstrated using the thinner 10 μm mats, while the added benefits of reduced scatter and further increase in interlaminar fracture properties tend to favor the use of slightly thicker mats (20 μm).

It is to be expected that an increase in interlaminar fracture toughness does not result in an equivalent increase in crash performance. The complexity of compressive crushing of corrugated structures is characterized by multiple concurrent failure modes, and although interlaminar fracture accounts only for a fraction of the total dissipated energy, it can be easily modified without resorting to a change of material. It is known, in fact, that the energy dissipated by the fiber fracture is several orders of magnitude higher than that absorbed by the interlaminar failure. However, different design requirements could influence the choice of composite's constituents and, therefore, this would not always be the best-suited for the crashworthiness property of the component.

4.3. Crush morphology

Fig. 12 and Fig. 13 show the macroscopic fracture morphology for each sample type. In Fig. 14, the crushing mechanisms and distinct fracture zones found in crushed corrugated composite profiles are

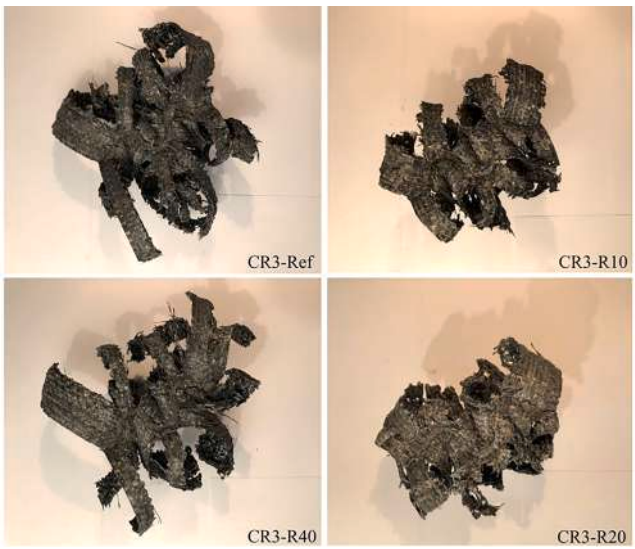

Fig. 12. Top view of CR3 specimens after crushing (one specimen per material configuration is shown).

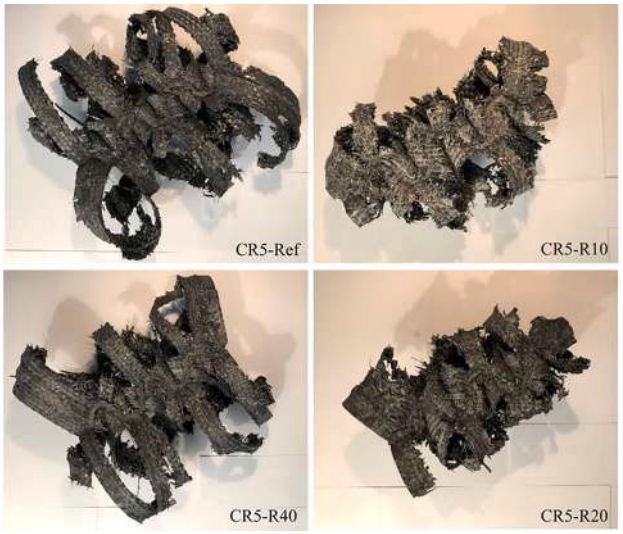

Fig. 13. Top view of CR5 specimens after crushing (one specimen per material configuration is shown).

highlighted. A central bundle wedge, formed by crushed fibers and matrix, can be identified along the profile midplane. The central delamination generates two fronds splaying outwards from the profile section, folding and crumbling due to friction against the crush plate. Fiber tearing between adjacent bundles is determined by the curvature of the profile and is not affected by the interlayer composition; in fact, no significant difference is evidenced in the number of individual bundles splaying from the midsection.

Moreover, on these fiber bundles, it can be observed that the reference and 40 μm reinforced crushed samples are characterized by fronds that tend to splay outwards with a large radius. Instead, the fronds in 10 and 20 μm reinforced samples are fragmented and tend to curl with a smaller radius. A closer inspection reveals that multiple interlaminar shearing fractures characterize the curl of the lamina bundles. These cracks highlight the leading role of the shear-cracking failure mode (Mode II) against the opening mode (Mode I) in the crushing failure of a composite coupon, as highlighted by Cauchi-Savona in [8]. In the 10 and 20 μm configurations, the tighter curvature of the lamina bundles is accompanied by higher crack density, which contributes to the

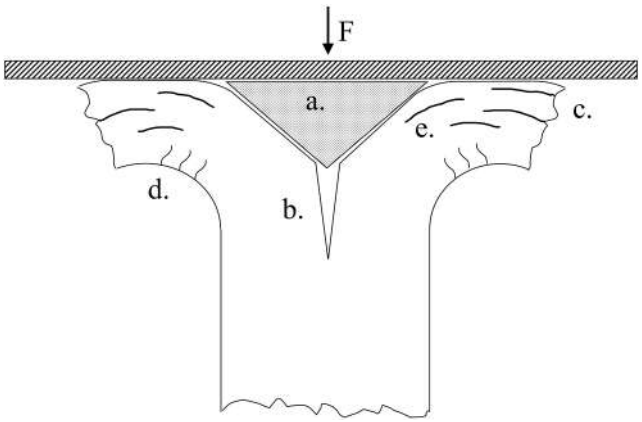

Fig. 14. Schematic representation of the fracture morphology and failure modes in the crush process zone: a. central debris bundle wedge; b. midplane delamination; c. splaying lamina bundle; d. compressive failure in bent laminae, e. shear delaminations in lamina bundles.

increased sustained load.

Another remarkable characteristic was, the higher amount of dispersed debris released during crushing in the reference samples, compared to the nano-reinforced configurations, where, on the contrary, fragments tend to remain attached to the coupon. This phenomenon can ascribed by the rubber content, which extends the epoxy resin plasticity and acts as a sticking agent, thus helping to hold together small particles.

Fig. 15 shows SEM micrographs taken from DCB delamination surfaces. As expected, the original nanofibrous morphology is completely lost in rubbery-modified laminates due to the thermal properties of NBR and PCL (low T_g and low melting temperature, respectively [36]). While pristine CFRP displays the typical brittle behavior of epoxies, characterized by wide flat fracture planes (Fig. 15a), rubbery-modified interfaces show a more corrugated matrix region (Fig. 15b,c,d). In addition, the fracture surface becomes more irregular, showing rounded recesses due to the ductile deformation by increasing the nanofibrous mat thickness. Furthermore, in the modified samples the decohesion between matrix and fiber is less pronounced and absent for higher reinforcement contents (Fig. 15c,d).

The SEM micrographs of the Mode II fracture surfaces revealed by ENF testing are reported in Fig. 16, where the different morphologies found around fibers oriented parallel (top row) and orthogonal (bottom row) to the crack tip are distinguished. Here, the effect of the nano-reinforcement on the fracture morphology is evident: the shear bands and microcrack formations (Fig. 16a,e) typically observed in epoxy resins are substituted, at the lowest reinforcement thickness, by an inhomogeneous fracture surface characterized by fragmentation into smaller particles (Fig. 16b). On the other hand, the higher mat thicknesses generate burr-like features, hinting at regions of the material which experienced substantial plastic deformation (Fig. 16c,d,f,g). Furthermore, the fiber–matrix decohesion due to pull-out from shear

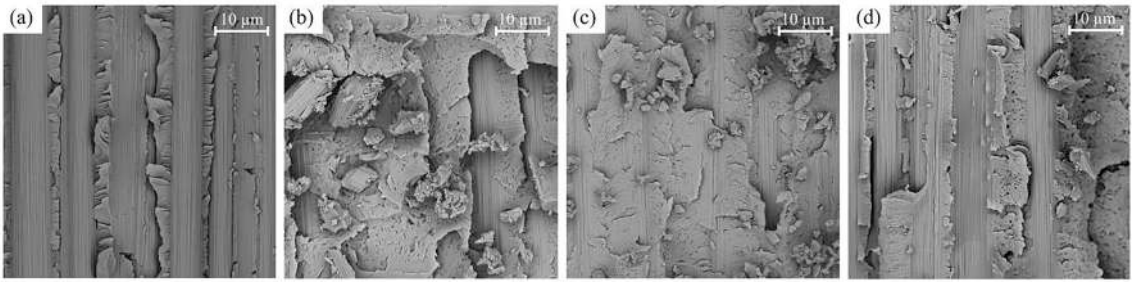

Fig. 15. SEM micrographs of delaminated surfaces recorded after DCB tests: Reference (a), R10 (b), R20 (c), R40 (d). The fracture propagation direction is from bottom to top.

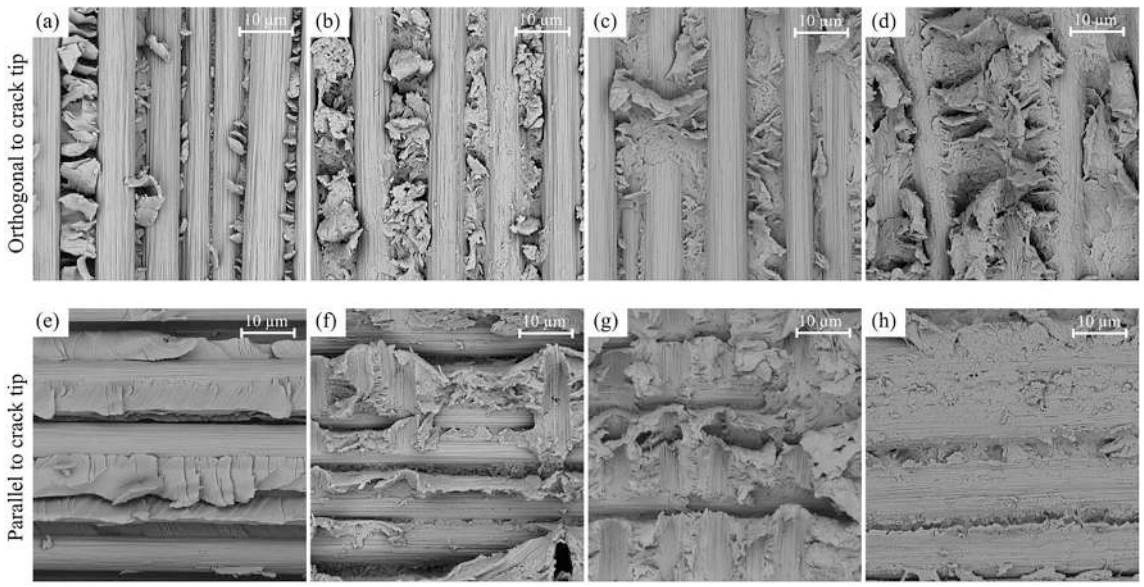

Fig. 16. SEM micrographs of delaminated surfaces recorded after ENF tests: fibers orthogonal to the crack tip (top row), and fibers parallel to the crack tip (bottom row). Reference (a,e), R10 (b,f), R20 (c,g), R40 (d,h). The fracture propagation direction is from bottom to top.

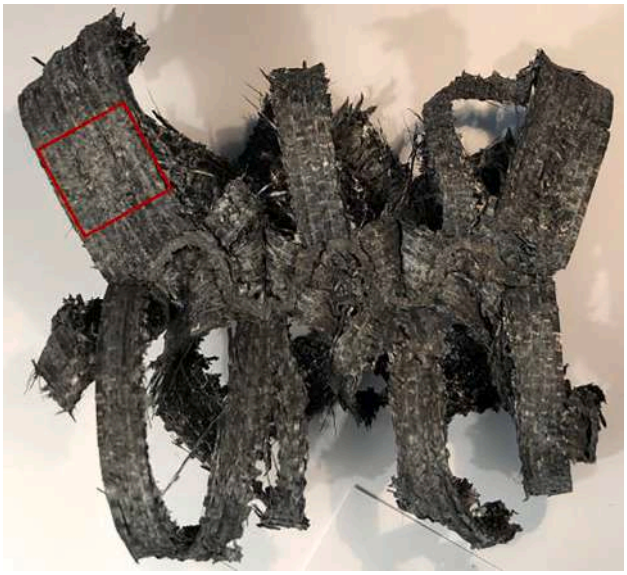

Fig. 17. Top view of a compressive crush coupon after testing. The region of the sample extracted for SEM analysis is highlighted.

loading seen in the reference material (Fig. 16e) is reduced at lower reinforcement content (R10 and R20) and completely suppressed in the R40 configuration (Fig. 16h).

For crush specimens, SEM coupons are extracted from lateral fronds of the crushed coupons, as shown in Fig. 17. Fig. 18 shows typical morphologies found in crushed CR5 specimens; CR3 images are not displayed due to their similarities. The presence of wide flat fracture planes is retrieved in the unmodified laminate (CR5-Ref), confirming the fragile behavior of the resin. Nano-reinforced coupons show a more irregular surface, which becomes more pronounced by increasing the mat thickness, thus confirming the ability of rubbery membranes to plasticize the resin and impart extensive plastic deformation in the toughened matrix. The specimens that exhibited higher energy absorption, CR5-R10 and CR5-R20, are characterized by carbon fibers well embedded in the epoxy resin. The plastic behavior of the resin and the optimal adhesion between the carbon fibers and the resin have contributed to increased crush resistance. When the thickest nanofibrous mat, R40, is integrated, a less adhesion of carbon fibers to the toughened matrix is observed. This fact is consistent with the lower crush resistance of the R40 samples: the poor adhesion of the carbon fibers to the matrix and the plastic behavior of the resin may promote buckling of the carbon fibers themselves, which could explain the lower SEA values.

5. Comparison with literature data

5.1. Interlaminar fracture toughness

The fracture toughness achieved by integrating the current NBR/PCL rubbery mats are compared with literature data in Fig. 19. Common nanofibers used against delamination are made by thermoplastics, such as polyamides (Nylons), PCL, and polyvinylidene fluoride (PVDF) [29,35,50]. Besides these, also other polymers can be used to increase the intrinsic resistance to delamination. As an example, polyethylene oxide (PEO), which finds an extensive application in medicine and healthcare, was recently reported as an effective nanofibrous medium for contrasting delamination, up to +221% in G_I [51]. Rubbery nanofibers were first proposed in 2020 for enhancing the interlaminar fracture toughness of CFRPs, achieving up to +480% in G_I [36]. Regarding

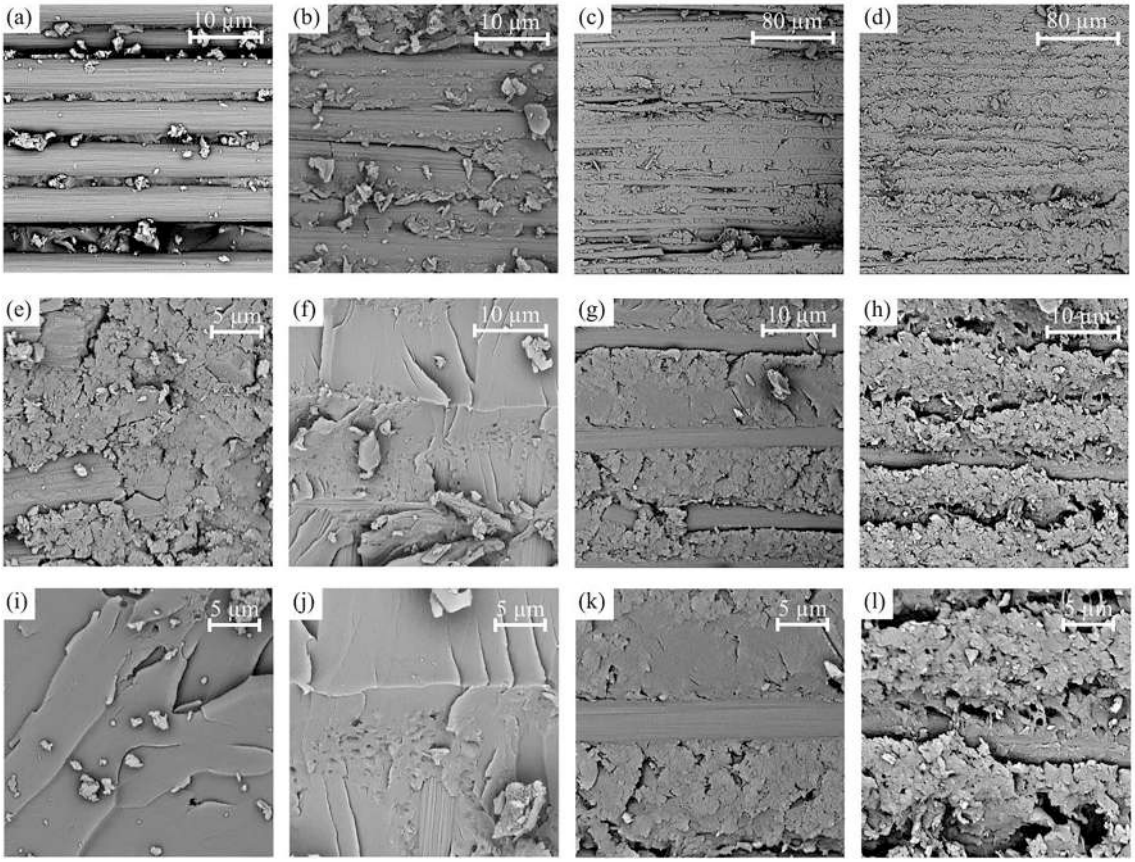

Fig. 18. SEM micrographs of delaminated surfaces for CR5 specimens after crushing tests. Reference (a,e,i), R10 (b,f,j), R20 (c,g,k), R40 (d,h,l).

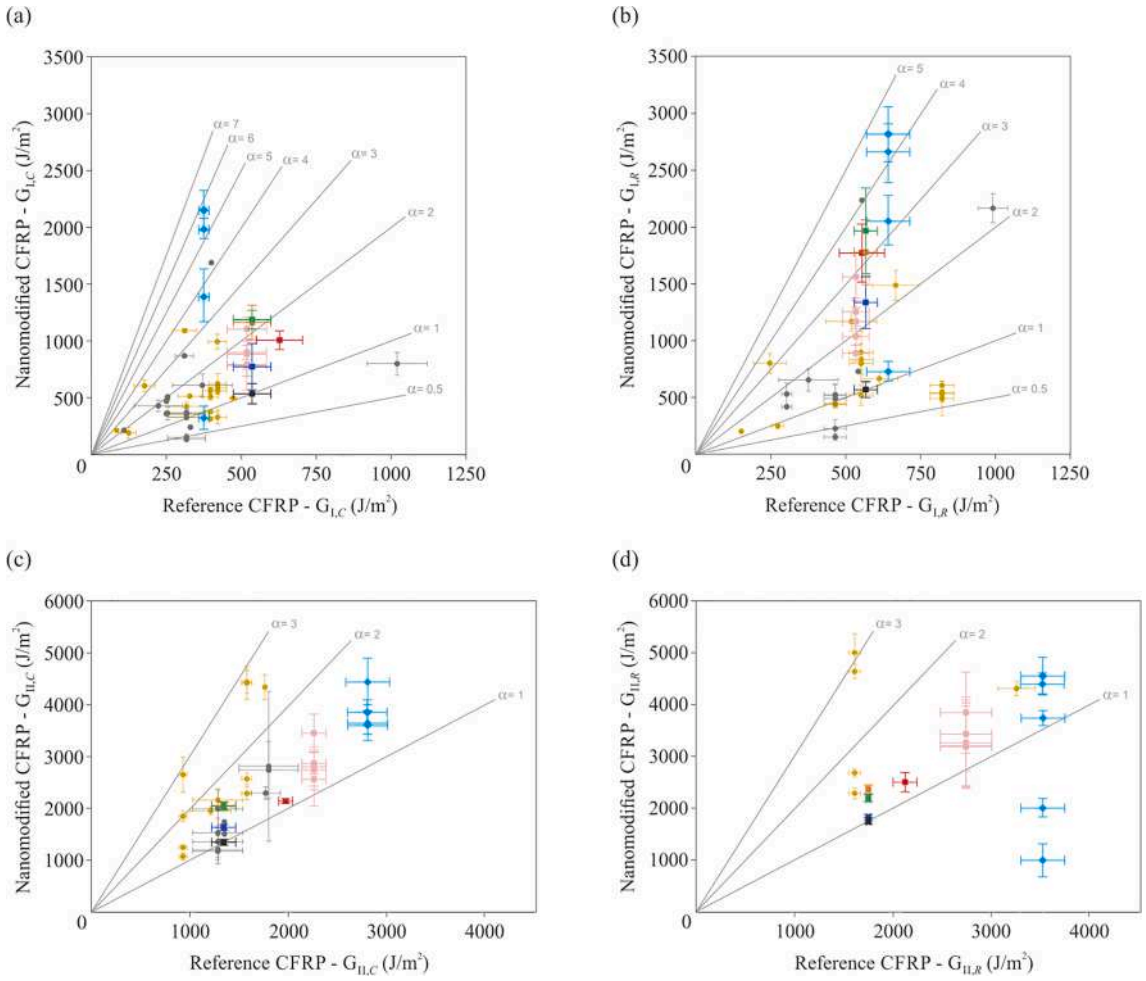

Fig. 19. Comparison of Mode I (a, b) and Mode II (c, d) energy release rate of tested composites (black Ref., blue R10, orange R20, and green R40) with literature data: yellow polyamide nanofibers, [35]; cyan, NBR/PCL nanofibers previously integrated in a different epoxy system [36]; cyan, NBR/Nomex nanofibers [30]; red, PEO nanofibers [51]; grey, "other" nanofiber types [35].

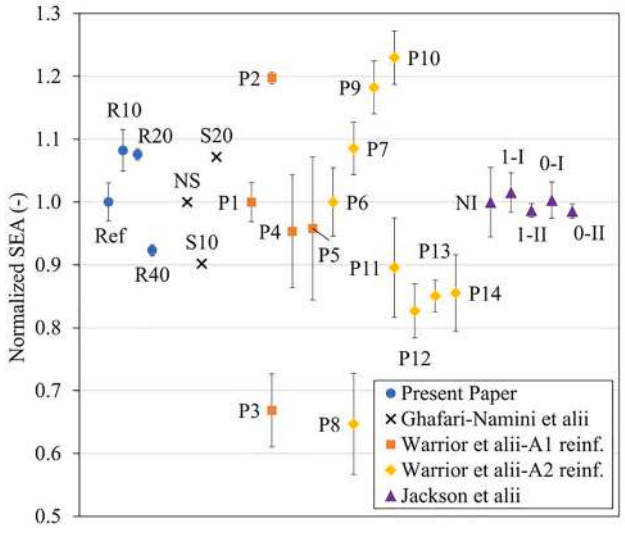

Fig. 20. Comparison of obtained SEA with literature data: blue dots, present paper; black cross points, [52]; orange squares, R1-resin/A1-fabric laminate [31]; yellow diamonds, R1-resin/A2-fabric laminate [31]; purple triangles, [53]. Results are normalized to the baseline value for each group. Standard deviations are shown where reported.

Mode I delamination, the results delivered by NBR/PCL blend nanofibers outperform, in almost all cases, the reinforcement provided by common polymers, such as polyamides which generally provide enhancements near 50–60%. The mat used in the present work, containing a 60% wt of NBR, provides a maximum increase in G_I of 254%. This enhancement is sensibly lower than the maximum one previously found (+480%) [36]; however, a different epoxy resin is used here. The boost in G_{II} provided by NBR/PCL nanofibers is mostly similar to common thermoplastic nanofibers and NBR/Nomex rubbery ones.

5.2. Crashworthiness SEA

Fig. 20 compares the results obtained in the present study with some outcomes found in the literature related to enhancing methods for crashworthiness properties. Stitching (flax yarns [52] and Kevlar 29 threads [31], with differen stitching patterns), thermoplastic film interleaf (80 μm urethane film [31] and polyimide film coated with a B-staged modified acrylic [53]), and thermoplastic polyester powder [31] are considered. All the results shown in Fig. 20, are normalized to the reference laminates to better compare different materials and geometries. Data from [31] is normalized with respect to the two kinds of fabric studied (A1, E-glass continuous filament random mat, and A2, E-glass non-crimp fabric); moreover, only results of one resin system (R1, polyester) are considered.

It is to highlight that the majority of the analyzed results are in agreement with the values obtained in this work: only the Kevlar 29

stitched coupons with the A1-fabric (P9 and P10 points) show higher SEA values. The same kind of stitching used on A2-fabric laminate led to a decrease of SEA (P4-5) Both the thermoplastic film interleaf and powder addition, for all the weight percentages studied in [31], show a decrease of the crush energy absorption (P8 and P11-14 points, respectively); also in [53] the use of film reinforcements does not lead to a significant SEA variation (purple triangles in the graph). Lastly, flax yarn stitching shows an increment for the 20 mm distant stitching line (S20) but a decrement for the closer one (S10), with respect to the non stitched result (NS). However, it does not exceed the values obtained in this work.

The NBR/PCL nanofibrous mat reinforcement, therefore, represent a better interface enhancement than films and powder additions. On the other hand, stitching could result in higher SEA increment, depending on the fabric; it represents, however, an increased complexity in the production and a limitation in the components' geometries.

6. Conclusions

Rubbery-modified epoxy CFRP laminates were tested under Mode I, Mode II, and compressive crush loading. In particular, elastomeric nanofibrous mats, made of NBR/PCL blend (60%wt of rubber), were interleaved, resulting in a relevant toughening improvement. Mode I fracture toughness increases up to 125% and 254% compared to the unmodified laminate for the initial and propagation stages, respectively. Mode II improvement is more limited but still significant: G_{II} is up to 47% higher than the reference material. In the compressive crush tests, the nanofibrous mats increment the SEA around 8% for the CFRPs modified with 10 and 20 μm mat thicknesses. On the contrary, the 40 μm mat causes a global reduction in the energy absorption capability of the material, lower than the one displayed by the unmodified laminate (-8%). SEM analysis revealed a high plasticization of the resin, which becomes higher for increasing the nanofibrous mat thickness, thanks to the NBR/PCL mixing with the hosting resin.

In terms of crush morphology, the addition of nanofibrous mats does not alter the macroscopic characteristics of the crushed lamina bundles considerably; nevertheless, all the nano-reinforced samples show a lower amount of dispersed debris, and, in the 10 and 20 μm configurations, a higher density of fractures, which contributes to improving the energy absorption. Tests demonstrated that integrating 10 and 20 μm mats effectively increases the SEA of a self-supporting geometry made of CFRP. This outcome is supported by the SEM micrographs, showing an improved adhesion at the fiber–matrix interface. An additional benefit of using mats of higher thickness is the reduction in the variability of SEA across multiple tests.

Such encouraging results demonstrate the feasibility of interleaving elastomeric nanofibers for increasing both interlaminar fracture toughness and SEA of CFRP laminates, paving the way for using these materials in a wide range of applications.

Funding

Financed by the projects: "TEAM SAVE—E91B18000460007" (PG/2018/632196) POR FESR 2014–2020 action by Regione Emilia Romagna; the European Union-NextGenerationEU (National Sustainable Mobility Center CN00000023, Italian Ministry of University and Research Decree n.1033-17/06/2022, Spoke n.1-Air mobility, Spoke n.5-Light vehicle and active mobility, Spoke n.11-Innovative Materials & Lightweighting); National Recovery and Resilience Plan (NRRP), Mission 04 Component 2 Investment 1.5–NextGenerationEU, Call for tender n.3277 dated 30/12/2021 (Award Number: 0001052 dated 23/06/2022).

CRediT authorship contribution statement

Maria Pia Falaschetti: Conceptualization, Methodology, Formal analysis, Investigation, Data curation, Writing – original draft. **Francesco Rondina:** Conceptualization, Methodology, Validation, Formal analysis, Investigation, Writing – original draft. **Emanuele Maccaferri:** Methodology, Formal analysis, Resources, Writing – review & editing. **Laura Mazzocchetti:** Conceptualization, Methodology, Resources, Writing – review & editing. **Lorenzo Donati:** Methodology, Supervision, Writing – review & editing, Funding acquisition. **Andrea Zucchelli:** Methodology, Writing – review & editing, Project administration, Funding acquisition. **Loris Giorgini:** Methodology, Supervision, Project administration, Funding acquisition.

Declaration of Competing Interest

The authors declare that they have no known competing financial interests or personal relationships that could have appeared to influence the work reported in this paper.

Data availability

The data that has been used is confidential.

Appendix A. Supplementary material

Supplementary data to this article can be found online at https://doi.org/10.1016/j.compstruct.2023.116845.

References

[1] Troiani E, Falaschetti MP, Taddia S, Ceruti A. CFRP crash absorbers in small UAV: design and optimization. In: SAE Tech. Pap., vol. 2015- Septe, SAE International; 2015. doi: 10.4271/2015-01-2461.
[2] Belingardi G, Chiandussi G. Vehicle crashworthiness design — general principles and potentialities of composite material structures. In: CISM Int. Cent. Mech. Sci. Courses Lect., vol. 526, Springer, Vienna; 2011, p. 193–264. doi: 10.1007/978-3-7091-0523-8_5.
[3] Thornton PH. Energy absorption in composite structures. J Compos Mater 1979;13:247–62. https://doi.org/10.1177/002199837901300308.
[4] Mamalis AG, Robinson M, Manolakos DE, Demosthenous GA, Ioannidis MB, Carruthers J. Crashworthy capability of composite material structures. Compos Struct 1997;37:109–34. https://doi.org/10.1016/S0263-8223(97)80005-0.
[5] Mamalis AG, Manolakos DE, Ioannidis MB, Papapostolou DP. On the experimental investigation of crash energy absorption in laminate splaying collapse mode of FRP tubular components. Compos Struct 2005;70:413–29. https://doi.org/10.1016/J.COMPSTRUCT.2004.09.002.
[6] Jiang H, Ren Y, Gao B. Research on the progressive damage model and trigger geometry of composite waved beam to improve crashworthiness. Thin-Walled Struct 2017;119:531–43. https://doi.org/10.1016/j.tws.2017.07.004.
[7] Troiani E, Donati L, Molinari G, Di Sante R. Influence of plying strategies and trigger type on crashworthiness properties of carbon fiber laminates cured through autoclave processing. Stroj Vestnik/J Mech Eng 2014;60:375–81. https://doi.org/10.5545/SV-JME.2013.1506.
[8] Cauchi Savona S, Hogg PJ. Effect of fracture toughness properties on the crushing of flat composite plates. Compos Sci Technol 2006;66:2317–28. https://doi.org/10.1016/J.COMPSCITECH.2005.11.038.
[9] Thornton PH, Harwood JJ, Beardmore P. Fiber-reinforced plastic composites for energy absorption purposes. Compos Sci Technol 1985;24:275–98. https://doi.org/10.1016/0266-3538(85)90026-0.
[10] Price JN, Hull D. Axial crushing of glass fibre-polyester composite cones. Compos Sci Technol 1987;28:211–30. https://doi.org/10.1016/0266-3538(87)90003-0.
[11] Feraboli P. Development of a corrugated test specimen for composite materials energy absorption. J Compos Mater 2008;42:229–56. https://doi.org/10.1177/0021998307086202.
[12] Ramakrishna S, Hamada H. Energy absorption characteristics of crash worthy structural composite materials. Key Eng Mater 1998;141–143:585–620. https://doi.org/10.4028/www.scientific.net/kem.141-143.585.
[13] Ghasemnejad H, Hadavinia H, Aboutorabi A. Effect of delamination failure in crashworthiness analysis of hybrid composite box structures. Mater Des 2010;31:1105–16. https://doi.org/10.1016/j.matdes.2009.09.043.
[14] Ramakrishna S, Hamada H, Maekawa Z, Sato H. Energy absorption behavior of carbon-fiber-reinforced thermoplastic composite tubes. J Thermoplast Compos Mater 1995;8:323–44. https://doi.org/10.1177/089270579500800307.
[15] Jacob GC, Fellers JF, Simunovic S, Starbuck JM. Energy absorption in polymer composites for automotive crashworthiness. J Compos Mater 2002;36:813–50. https://doi.org/10.1177/0021998302036007164.
[16] Carruthers JJ, Kettle AP, Robinson AM. Energy absorption capability and crashworthiness of composite material structures: a review. Appl Mech Rev 1998;51:635–49. https://doi.org/10.1115/1.3100758.

[17] CMH-17. Composite materials handbook. SAE International; n.d.
[18] Mamalis AG, Manolakos DE, Demosthenous GA, Ioannidis MB. Crashworthiness of Composite Thin-Walled Structures. 1998.
[19] Cauchi Savona S, Hogg PJ. Investigation of plate geometry on the crushing of flat composite plates. Compos Sci Technol 2006;11–12:1639–50. https://doi.org/10.1016/J.COMPSCITECH.2005.11.011.
[20] Hanagud S, Craig JI, Sriram P, Zhou W. Energy absorption behavior of graphite epoxy composite sine webs. J Compos Mater 1989;23:448–59. https://doi.org/10.1177/002199838902300502.
[21] Farley GL, Jones RM. Crushing characteristics of continuous fiber-reinforced composite tubes. J Compos Mater 1992;26:37–50. https://doi.org/10.1177/002199839202600103.
[22] Hull D. A unified approach to progressive crushing of fibre-reinforced composite tubes. Compos Sci Technol 1991;40:377–421. https://doi.org/10.1016/0266-3538(91)90031-J.
[23] Farley GL, Jones RM. Prediction of the energy-absorption capability of composite tubes. J Compos Mater 1992;26:388–404. https://doi.org/10.1177/002199839202600304.
[24] Hamada H, Coppola JC, Hull D, Maekawa Z, Sato H. Comparison of energy absorption of carbon/epoxy and carbon/PEEK composite tubes. Composites 1992;23:245–52. https://doi.org/10.1016/0010-4361(92)90184-V.
[25] Robinette EJ, Ziaee S, Palmese GR. Toughening of vinyl ester resin using butadiene-acrylonitrile rubber modifiers. Polymer (Guildf) 2004;45:6143–54. https://doi.org/10.1016/j.polymer.2004.07.003.
[26] Fakhar A, Seyed Salehi M, Keivani M, Abadyan M. Comprehensive study on using VTBN reactive oligomer for rubber toughening of epoxy resin and composite. Polym Plast Technol Eng 2016;55:343–55. https://doi.org/10.1080/03602559.2015.1098677.
[27] Dransfield KA, Jain LK, Mai YW. On the effects of stitching in CFRPs—I. mode I delamination toughness. Compos Sci Technol 1998;58:815–27. https://doi.org/10.1016/S0266-3538(97)00229-7.
[28] Göktaş D, Kennon WR, Potluri P. Improvement of Mode I interlaminar fracture toughness of stitched glass/epoxy composites. Appl Compos Mater 2017;24:351–75. https://doi.org/10.1007/S10443-016-9560-X/TABLES/11.
[29] Zheng N, Liu HY, Gao J, Mai YW. Synergetic improvement of interlaminar fracture energy in carbon fiber/epoxy composites with nylon nanofiber/polycaprolactone blend interleaves. Compos Part B Eng 2019;171:320–8. https://doi.org/10.1016/J.COMPOSITESB.2019.05.004.
[30] Maccaferri E, Mazzocchetti L, Benelli T, Brugo TM, Zucchelli A, Giorgini L. Self-assembled NBR/nomex nanofibers as lightweight rubbery nonwovens for hindering delamination in epoxy CFRPs. ACS Appl Mater Interfaces 2022;14:1885–99. https://doi.org/10.1021/ACSAMI.1C17643/SUPPL_FILE/AM1C17643_SI_001.PDF.
[31] Warrior NA, Turner TA, Robitaille F, Rudd CD. The effect of interlaminar toughening strategies on the energy absorption of composite tubes. Compos Part A Appl Sci Manuf 2004;35:431–7. https://doi.org/10.1016/J.COMPOSITESA.2003.11.001.
[32] Mouritz AP, Leong KH, Herszberg I. A review of the effect of stitching on the in-plane mechanical properties of fibre-reinforced polymer composites. Compos Part A Appl Sci Manuf 1997;28:979–91. https://doi.org/10.1016/S1359-835X(97)00057-2.
[33] Yudhanto A, Watanabe N, Iwahori Y, Hoshi H. Effect of stitch density on tensile properties and damage mechanisms of stitched carbon/epoxy composites. Compos Part B Eng 2013;46:151–65. https://doi.org/10.1016/J.COMPOSITESB.2012.10.003.
[34] Povolo M, Maccaferri E, Cocchi D, Brugo TM, Mazzocchetti L, Giorgini L, et al. Damping and mechanical behaviour of composite laminates interleaved with rubbery nanofibers. Compos Struct 2021;272:114228. https://doi.org/10.1016/J.COMPSTRUCT.2021.114228.
[35] Palazzetti R, Zucchelli A. Electrospun nanofibers as reinforcement for composite laminates materials – a review. Compos Struct 2017;182:711–27. https://doi.org/10.1016/J.COMPSTRUCT.2017.09.021.
[36] Maccaferri E, Mazzocchetti L, Benelli T, Brugo TM, Zucchelli A, Giorgini L. Rubbery nanofibrous interleaves enhance fracture toughness and damping of CFRP laminates. Mater Des 2020;195:109049. https://doi.org/10.1016/j.matdes.2020.109049.
[37] An D, Lotfian S, Mesbah D, Ayre D, Yoosefinejad A, Thakur VK, et al. Ultra-thin electrospun nanofibers for development of damage-tolerant composite laminates. Mater Today Chem 2019;14:100202. https://doi.org/10.1016/J.MTCHEM.2019.100202.
[38] Zucchelli A, Focarete ML, Gualandi C, Ramakrishna S. Electrospun nanofibers for enhancing structural performance of composite materials. Polym Adv Technol 2011;22:339–49. https://doi.org/10.1002/PAT.1837.
[39] Maccaferri E, Mazzocchetti L, Benelli T, Brugo TM, Zucchelli A, Giorgini L. Rubbery nanofibers by co-electrospinning of almost immiscible NBR and PCL blends. Mater Des 2020;186:108210. https://doi.org/10.1016/J.MATDES.2019.108210.
[40] Zhang X, Chase GG. Electrospun elastic acrylonitrile butadiene copolymer fibers. Polymer (Guildf) 2016;97:440–8. https://doi.org/10.1016/J.POLYMER.2016.05.063.
[41] Thielke MW, Bruckner EP, Wong DL, Theato P. Thiol-ene modification of electrospun polybutadiene fibers crosslinked by UV irradiation. Polymer (Guildf) 2014;55:5596–9. https://doi.org/10.1016/J.POLYMER.2014.09.002.
[42] Zhang X, Yang X, Chase GG. Filtration performance of electrospun acrylonitrile-butadiene elastic fiber mats in solid aerosol filtration. Sep Purif Technol 2017;186:96–105. https://doi.org/10.1016/J.SEPPUR.2017.06.002.
[43] Kerr-Phillips TE, Woehling V, Agniel R, Nguyen GTM, Vidal F, Kilmartin P, et al. Electrospun rubber fibre mats with electrochemically controllable pore sizes. J Mater Chem B 2015;3:4249–58. https://doi.org/10.1039/C5TB00239G.
[44] Liu H-Y, Hsieh H-C, Chen J-Y, Shih C-C, Lee W-Y, Chiang Y-C, et al. Fabrication and application of highly stretchable conductive fiber-based electrode of epoxy/NBR electrospun fibers spray-coated with AgNW/PU composites. Macromol Chem Phys 2019;220:1800387. https://doi.org/10.1002/MACP.201800387.
[45] Rondina F, Donati L. Comparison and validation of computational methods for the prediction of the compressive crush energy absorption of CFRP structures. Compos Struct 2020;254:112848. https://doi.org/10.1016/j.compstruct.2020.112848.
[46] Rondina F, Falaschetti MP, Zavatta N, Donati L. Numerical simulation of the compression crushing energy of carbon fiber-epoxy woven composite structures. Compos Struct 2022::116300. https://doi.org/10.1016/J.COMPSTRUCT.2022.116300.
[47] Maccaferri E, Cocchi D, Mazzocchetti L, Benelli T, Brugo TM, Giorgini L, et al. How nanofibers carry the load: toward a universal and reliable approach for tensile testing of polymeric nanofibrous membranes. Macromol Mater Eng 2021;306:2100183. https://doi.org/10.1002/mame.202100183.
[48] ASTM standard. ASTM D5528–13: Standard test method for mode I interlaminar fracture toughness of unidirectional fiber-reinforced polymer matrix composites. Am Stand Test Methods 2014;03:1–12.
[49] ASTM standard. ASTM D7905: Standard test method for determination of the mode II interlaminar fracture toughness of unidirectional fiber-reinforced polymer matrix composites. ASTM 2014:1–18.
[50] Daelemans L, Van Der Heijden S, De Baere I, Rahier H, Van Paepegem W, De Clerck K. Damage-resistant composites using electrospun nanofibers: a multiscale analysis of the toughening mechanisms. ACS Appl Mater Interfaces 2016;8:11806–18. https://doi.org/10.1021/ACSAMI.6B02247/ASSET/IMAGES/LARGE/AM-2016-022476_0013.JPEG.
[51] Maccaferri E, Ortolani J, Mazzocchetti L, Benelli T, Brugo TM, Zucchelli A, et al. New application field of polyethylene oxide: PEO nanofibers as epoxy toughener for effective CFRP delamination resistance improvement. ACS Omega 2022;7:23189–200. https://doi.org/10.1021/ACSOMEGA.2C01189/ASSET/IMAGES/LARGE/AO2C01189_0009.JPEG.
[52] Ghafari-Namini N, Ghasemnejad H. Effect of natural stitched composites on the crashworthiness of box structures. Mater Des 2012;39:484–94. https://doi.org/10.1016/J.MATDES.2012.03.025.
[53] Jackson A, Dutton S, Gunnion AJ, Kelly D. Effect of manufacture and laminate design on energy absorption of open carbonfibre/ epoxy sections. ICCM17, Edinburgh (UK); 2009.